# Mechanism of uranium(VI) sorption on α-aminophosphonate sorbents: multimodal spectroscopy and computational study

Ahmed M. A. El-Seidy, [ID] *[a] Ibrahim E. El-Sayed,[b] Mikko Linnolahti [ID] *[c]
Eman E. Bayoumi,[d] Hamed I. Mira[d] and Ahmed A. Galhoum*[d]

Carbon-free nuclear energy meets growing energy demand; uranium recycling enhances sustainability, economic, and environmental benefits. Herein, efficient three α-aminophosphonates-based sorbents were previously synthesized *via* a one-pot method using distinct amine precursors (aniline, *O*-phenylenediamine, anthranilic acid), yielding S–H, S–NH$_2$ aminated, and S–COOH carboxylated, respectively enhanced aminophosphonate. Elemental analysis confirms three α-aminophosphonate sorbents (S–H, S–COOH, S–NH$_2$) with amine-dependent structures. Optimal U(VI) sorption was observed at pH 4.0, 25 ± 1 °C, and 90 min contact time, with Langmuir-derived capacities ($q_m$) of 1.312, 0.762, and 0.601 mmol U per g for S–H, S–NH$_2$, and S–COOH, respectively. Multimodal characterization combining FTIR, XPS, and SEM-EDX with Density Functional Theory (DFT) simulations elucidated structure–property relationships and binding mechanisms *via* integrated experimental/computational analysis. FTIR analysis of uranyl-loaded sorbents (S–H–U, S–NH$_2$–U, S–COOH–U) revealed inner-sphere U(VI) complexation *via* nitrogen (>NH/−NH$_2$) and oxygen (P=O, P–O–Ph) ligands, modulated to probe coordination environments and redox behavior. XPS revealed ligand-dependent redox selectivity: S–H–U retained 46.30% U(VI), whereas S–NH$_2$–U and S–COOH–U preferentially stabilized U(IV) (61.44–86.69%), underscoring tunable uranium speciation. Enamine–imine tautomerism at bridging >NH sites dictated U(VI) coordination geometry. SEM-EDX analysis correlated enhanced U(IV) sorption with nanoscale/hierarchical surface roughness, while post-sorption morphological changes confirmed active-site saturation and morphology-governed sorption. DFT simulations validated experimental spectra, revealing U(VI) coordination geometries and energetics, where deprotonation states and functional group chemistry governed binding thermodynamics and stability. This study pioneers molecular-level design criteria for α-aminophosphonate sorbents through structure–property relationships connecting tailored functional group engineering (*e.g.*, >NH, P=O, −COOH) and surface-texture to optimize U(VI) binding energetics.

## 1 Introduction

Nuclear power provides carbon-free energy to meet rising global demand. Closed fuel cycles *via* uranium recycling offer enhanced sustainability through resource efficiency and reduced waste. Realizing these benefits requires advanced separation materials engineered for selective uranium recovery, a key challenge in nuclear materials science.[1,2] Uranium

*[a]Inorganic Chemistry Department, Advanced Materials Technology & Mineral Resources Research Institute, National Research Center, 33 El-Bohouth St., Dokki, P. O. 12622, Cairo, Egypt. E-mail: am.elseidy@nrc.sci.eg; ahmedmaee2@gmail.com*
*[b]Chemistry Department, Faculty of Science, Menoufia University, Egypt*
*[c]Department of Chemistry and Sustainable Technology, University of Eastern Finland, Joensuu Campus, 80101 Joensuu, Finland. E-mail: mikko.linnolahti@uef.fi*
*[d]Nuclear Materials Authority, P.O. Box 530, El-Maadi, Cairo, Egypt. E-mail: galhoum-nma@yahoo.com*

contamination in water resources is a pressing environmental issue due to its chemical toxicity and radiological hazards. Its presence, primarily as uranyl ions (UO$_2$$^{2+}$) in aqueous systems, poses significant risks to human health and ecosystems. Efficient removal strategies are therefore crucial, with sorption being a widely adopted and effective method.[3,4] Chelating sorbents are organic polymers equipped with specialized reactive groups designed to effectively bind and immobilize metal ions. Chelating resins, in line with the Hard and Soft Acid–Base theory (HSAB) by Pearson, exhibit properties influenced by the nature of metal ions. Uranium, characterized as a hard acid, displays a heightened attraction to hard bases. Consequently, chelating agents containing O, N, and P groups prove highly efficient in selectively sorbing uranium ions, offering high capacity and facilitating selective separation.[5–7] Recent emphasis has been placed on advancements in the design of organophosphorus ligands. These compounds exhibit excellent

metal-complexing properties, making them extensively utilized in large-scale industrial applications such as water treatment. Their effectiveness extends to the removal of radioactive and transition metals, contributing significantly to pollution control efforts.[5,7] Among the various sorbent materials explored, $\alpha$-aminophosphonate-based sorbents have gained attention for their high affinity towards uranium(VI) due to their functionalized surfaces and chelating capabilities.[6,7] Over the past few decades, aminophosphonates have consistently garnered significant interest from the research community. Notably, in the extraction of uranium from aqueous solutions-whether through solvent extraction or sorption on ion-exchange and chelating resins the efficacy of phosphorus groups, including TBP, phosphonate, and aminophosphonate, has proven highly efficient for the recovery of uranium.[5,6,8–10] To enhance the design of resins, the focus has been on incorporating phosphonate groups due to their advantageous properties. However, the reactivity of these groups is susceptible to changes in the chemical environment, influenced by induction effects, acid–base effects, or dual functionalities.

The sorption mechanism of uranium(VI) is governed by complex interactions between the sorbent's functional groups and uranyl ions. These interactions can involve coordination, ion exchange, and hydrogen bonding, which are influenced by factors such as pH, temperature, and the chemical nature of the sorbent. Despite significant advancements, the precise molecular mechanisms and the roles of specific functional groups remain areas of active research.[4,10]

This study delves into $\alpha$-aminophosphonate derivatives through a one-pot synthesis method, where amine precursors react directly with salicylaldehyde and triphenylphosphite.[7] The investigation evaluates the structure/activity relationship by examining uranyl sorption properties while varying the chemical environment of grafted amine, ranging from aniline (the 'simplest' aromatic amine) to anthranilic (amine *ortho*-substituted with a carboxylic acid or *o*-aminobenzoic acid) and *O*-phenylene diamine (*ortho*-aromatic diamine). To address these knowledge gaps, this study combines experimental and computational approaches to investigate uranium(VI) sorption mechanisms on $\alpha$-aminophosphonate sorbents. Surface complex structures can be identified through diverse spectroscopic methods, including X-ray photoelectron spectroscopy (XPS), infrared spectroscopy (FTIR), and computational calculations. Notably, experimental XPS and FTIR analyses are preferred techniques for their ability to probe chemical bonds. This study offers a comprehensive insight into the U(VI) sorption mechanism, employing advanced analytical tools and research methods to potentially enhance process efficiency.

Computational methods, particularly Density Functional Theory (DFT), provide molecular-level insights into the coordination environment of uranium(VI) with reactive groups, including amines, phosphonates, and hydroxyls.[11] This integrated approach aims to provide a comprehensive understanding of uranium(VI) binding mechanisms, offering valuable insights into the design of advanced sorbents for uranium remediation under environmental and industrial conditions. The research focuses on investigating the sorption mechanism of U(VI) ions on chelating sorbents with $\alpha$-aminophosphonate functional groups. By analyzing various sorbents before and after the U(VI) sorption process, the study aims to improve the understanding of the sorption mechanism on sorbents containing $\alpha$-aminophosphonate functional groups.
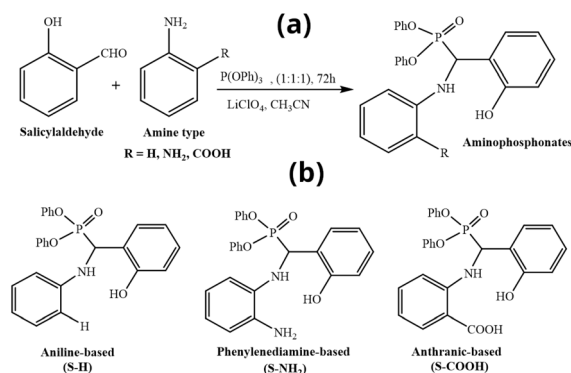
## 2 Experiments

### 2.1 Sorbent's synthesis

The sorbent was synthesized following Rashad *et al.*'s method[7] *via* a three-component reaction comprising: (1) amine substrate (1.00 mmol; aniline, *o*-phenylenediamine, or anthranilic acid), (2) salicylaldehyde (1.00 mmol), and (3) triphenyl phosphite (1.00 mmol) in acetonitrile (5.00 mL). The mixture was stirred at ambient temperature (10 min), followed by addition of $LiClO_4$ catalyst (20 mg) and continued stirring for 72 h. Scheme 1a illustrates the synthetic route, while Scheme 1b presents the proposed sorbents structures.

### 2.2 Sorbents loading

The experiments were performed at $25 \pm 1$ °C, sorbent dose (0.50 g L$^{-1}$) and the pH maintained at 4.0 with the equilibrium time was determined to be 40 min (but here extended to 24 h to obtain saturation level).[7]

### 2.3 Computational details

Density functional theory calculations were carried out by the metahybrid GGA functional M06-2X,[12] as employed previously for U(VI) complexes,[13] combined with the def-TZVP basis set by Ahlrics *et al.*[14] The M06-2X functional inherently includes dispersion corrections through its parameterization. For description of the core electrons of U, a relativistic effective core potential of 60 electrons was used.[15] Calculations were carried out in water medium by the SMD variation of the polarizable continuum model (PCM),[16] as implemented in Gaussian 16 software.[17] The SMD solvation model uses a dielectric constant of 78.36 for water at 298 K. Optimized structures were confirmed as true minima in the potential energy surface by harmonic vibrational frequency calculations. Gibbs free energies were calculated at $T = 298$ K and $p = 1$ atm and were



**Scheme 1** $\alpha$-aminophosphonate sorbents: (a) synthesis and (b) their chemical structure.

corrected for the low-energy vibrations by quasi-harmonic treatment of entropy[18] and enthalpy[19] with cut-off frequency of 100 cm$^{-1}$, and for the reduced translational entropy in solution.[20] The corrections were employed using Goodvibes script.[21] No scaling factors were employed.

### 2.4 Experimental techniques

XPS Analysis: High-resolution XPS spectra were acquired using a Thermo Fisher Scientific K-ALPHA spectrometer (Al Kα radiation, $h\nu = 1486.6$ eV) with a 400 μm spot size. Measurements were performed under ultrahigh vacuum ($10^{-9}$ mbar) with pass energies of 200 eV (survey scans) and 50 eV (high-resolution scans), covering a binding energy range of −10 to 1350 eV. Avantage (v6.5.1) was used for XPS fitting. Functional structural changes were documented using Attenuated Total Reflectance-Fourier Transform Infrared (FTIR) analysis within 4000–400 cm$^{-1}$ (FT/IR-6600. IRT-5200, JASCO Corporation, Tokyo, Japan). This SEM-EDX analysis was analyzed using Prisma E-SEM model (Thermo-Fisher Scientific Inc., Waltham, MA, USA), integrated with EDX unit (energy-dispersive X-ray spectroscopy). Quantitative elemental analysis (C, H, N) was performed via combustion-based microanalysis using a CHNS Vario EL III analyzer (Elementar, Germany).

## 3 Results and discussion

### 3.1 Elemental analysis

Elemental analysis validates the successful synthesis of three α-aminophosphonate sorbents (S–H, S–COOH, S–NH$_2$), with distinct structural features dictated by their amine precursors. The carbon content varies as S–H (63.92%) > S–NH$_2$ (62.79%) > S–COOH (61.15%). This trend reflects structural differences: S–H's pure aromatic core, S–COOH's carboxyl groups, and S–NH$_2$'s balanced diamine incorporation. Similarly, the nitrogen and hydrogen content trends reveal structural differences: S–NH$_2$'s elevated N (5.01%) and H (5.63%) content indicate free –NH$_2$ groups, while S–COOH's minimal values (4.01% N, 3.62% H) reflect carboxylate H-bonding networks. S–H's intermediate composition (4.94% N, 4.03% H) confirms its aniline-derived structure, demonstrating precise precursor control over sorbent chemistry. Oxygen content varies significantly: S–COOH shows the highest O% (23.97%) from carboxyl groups, while S–NH$_2$ has lowest (18.98%). S–H's intermediate O% (19.36%), reflecting precursor-dependent. Phosphorus levels remain consistent across sorbents (7.25–7.75%), confirming successful phosphonate incorporation. These compositional trends correlate with the molecular formulas and masses: S–H (C$_{25}$H$_{22}$NO$_4$P, 431.42 g mol$^{-1}$), S–COOH (C$_{26}$H$_{22}$NO$_6$P, 475.43 g mol$^{-1}$), and S–NH$_2$ (C$_{25}$H$_{23}$N$_2$O$_4$P, 446.43 g mol$^{-1}$). The data collectively demonstrate how precursor selection tailors sorbent chemistry for targeted applications.

### 3.2 Computational results and comparison to experiments

Binding of UO$_2^{2+}$ on the aniline-based (S–H), phenylenediamine-based (S–NH$_2$) and anthranilic-based (S–COOH) sorbents were carried by the M06-2X/def-TZVP method in water medium using the SMD variation of the polarizable continuum model, as described under computational details. The binding was considered taking place on each combination of O and N atoms of the sorbents and was studied under four scenarios: protonated vs. de-protonated sorbents, corresponding to lower vs. higher pH, combined with uranium: sorbent ratio of 1 : 1 vs. 1 : 2, corresponding to higher vs. lower U concentration. The binding was found exergonic for each sorbent and for each scenario, as shown in Fig. 1–3 for S–H, S–NH$_2$, and S–COOH, respectively, which illustrate the lowest free energy species located for each case and scenario.

The discussion begins from S–H (Fig. 1). At low pH and high U concentration, uranium forms a four-coordinate seesaw chelate to –P=O and to –C–OH, hydrogen of -C–OH transferring to the adjacent –NH– moiety. With calculated $\Delta G = -61.6$ kJ mol$^{-1}$, the binding is exergonic, and it goes further down by 14.8 kJ mol$^{-1}$ upon reaction with another S–H so that to form the thermodynamically preferred lower U concentration species having analogous binding modes, but octahedral six coordination for U. At higher pH, S–H is deprotonated from the –C–OH group, and hence in case of higher U concentration leads to binding analogous to lower pH, absent the hydrogen transfer. With calculated $\Delta G = -157.2$ kJ mol$^{-1}$, the binding is much more exergonic at higher pH and goes further down by 109.8 kJ mol$^{-1}$ at low U concentration, where the octahedral six coordination of U is further stabilized by dispersive interactions between the aromatic rings.

S–NH$_2$ and S–COOH follow the same patterns in terms of free energies (Fig. 2 and 3), which are more exergonic at higher pH and at lower U concentration, but the binding modes are generally different. At lower pH and higher U concentration, the binding mode is analogous to S–H, such that the additional –NH$_2$ group has little role. This is also seen in $\Delta G = -65.0$ kJ mol$^{-1}$, which is nearly the same as for S–H. However, at lower U concentration, the –NH$_2$ groups provide additional stabilization for the complex, binding to U along the –NH– and –P=O groups, hence leading to increase of U coordination from
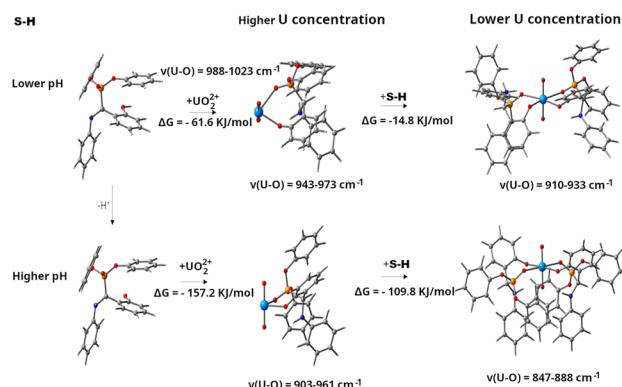


**Fig. 1** M06-2X/def-TZVP-optimized structures and Gibbs energies for binding of UO$_2^{2+}$ to S–H at varying pH and uranium concentration conditions in aqueous solution. Color coding: U (cyan), O (red), N (blue), P (orange), C (gray), H (white). Structural features: the uranyl unit (UO$_2^{2+}$) is shown as linear O=U=O with the central uranium atom coordinating to sorbent functional groups.
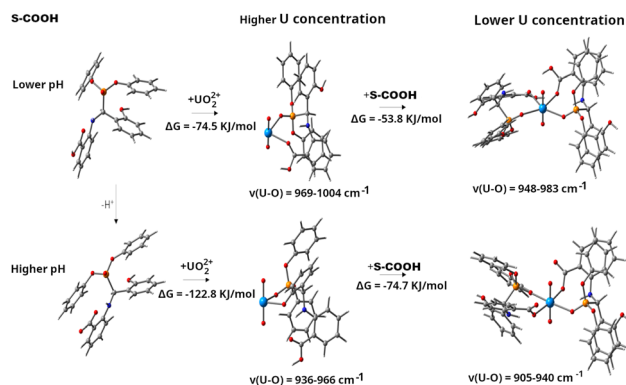
Fig. 2 M06-2X/def-TZVP-optimized structures and Gibbs energies for binding of $UO_2^{2+}$ to S−NH$_2$ at varying pH and uranium concentration conditions in aqueous solution. Color coding: U (cyan), O (red), N (blue), P (orange), C (gray), H (white). Structural features: the additional amine groups (−NH$_2$) in S−NH$_2$ provide extra coordination sites compared to S−H.
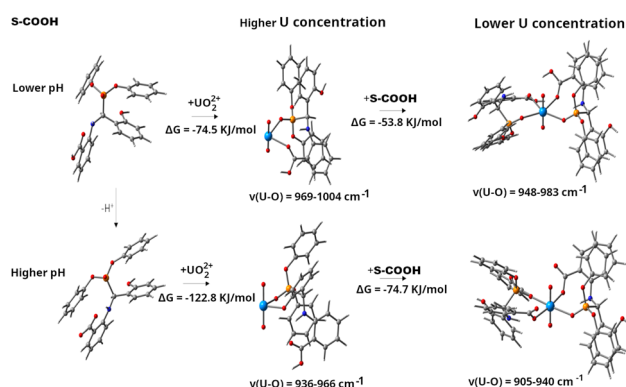


Fig. 3 M06-2X/def-TZVP-optimized structures and Gibbs energies for binding of $UO_2^{2+}$ to S−COOH at varying pH and uranium concentration conditions in aqueous solution. Color coding: U (cyan), O (red), N (blue), P (orange), C (gray), H (white). Structural features: the carboxyl group (−COOH) provides an additional oxygen-donor site with different electronic properties compared to hydroxyl groups.

six to eight. This effect is not seen at higher pH, where the sorbent, deprotonated from the −C−OH group, binds analogous to S−H. S−COOH, on the other hand, binds at lower pH from the carboxyl group along with -P=O, at both higher and lower U concentration, and with higher free energies than S−H and S−NH$_2$. However, at higher pH and lower U concentration, hydrogen transfers back to the deprotonated carboxyl group, leading to binding analogous to S−H and S−NH$_2$, whereas at lower U concentration the binding is analogous to lower pH, with octahedral six-coordination achieved *via* binding to −P=O and carboxyl groups.

Comparison of the sorption capabilities of the three sorbents is thus complicated by the dependence of the structural characteristics on the conditions. At lower pH the order in reaction Gibbs energies is S−H < S−NH$_2$ < S−COOH, at both U concentrations. At higher pH, the order is the opposite at both concentrations: S−COOH < S−NH$_2$ < S−H. Furthermore, reaction

Gibbs energies indicate that the reactivities are the highest at the combination of higher pH and lower U concentration.

The calculated binding free energies correlate well with experimental sorption capacities, though the relationship depends on pH and uranium concentration. At higher pH, the computed binding strength follows the order S−H > S−NH$_2$ > S−COOH, matching the experimental sorption capacities (1.31, 0.762, and 0.601 mmol U per g, respectively). However, at lower pH, calculations predict a reversed trend in binding energies (S−COOH > S−NH$_2$ > S−H), suggesting that optimal sorption conditions require pH control. The Coordinates of optimized geometries are given in SI Section I.

### 3.3 XPS

The XPS survey spectra of S−H, S−NH$_2$, S−COOH, S−H−U, S−NH$_2$−U and S−COOH−U are shown in Fig. 4a(i–ix). The spectra of all samples showed the presence of phosphorus (P-2p: 134.22–134.91 eV), carbon (C-1s: 285.35–286.05 eV), nitrogen (N-1s: 394.87–401.12 eV), and oxygen (O-1s: 532.27–533.73 eV) which support the composition of the basic structures. The spectra of S−H−U, S−NH$_2$−U and S−COOH−U (Fig. 4a(d–i)) show also the



Fig. 4 (a) The XPS survey spectra of (i) S−H, (ii) S−NH$_2$, (iii) S−COOH, (iv) S−H−U, (v) S−NH$_2$−U, (vi) S−COOH−U, and zoom spectra of: (vii) S−H−U, (viii) S−NH$_2$−U, and (ix) S−COOH−U, (b) XHRs of P-2p of (i) S−H, (ii) S−NH$_2$, (iii) S−COOH, (iv) S−H−U, (v) S−NH$_2$−U, (vi) S−COOH−U, (c) XHRs of S of (i) S−H−U, (ii) S−NH$_2$−U, and (iii) S−COOH−U.

presence of uranium (U-4d3: 781.28–783.08 eV, U-4d5: 741.08 eV, U-4f5: 393.08 eV, and U-4f7: 381.86–383.50 eV) and sulfur (S-2p: 167.63–168.25 eV). Excellent agreement was observed between fitted and experimental curves in all XPS high-resolution spectra (XHRs). The HRs of P-2p of all samples are shown in Fig. 4b(i–ix). These spectra show $2p_{frac32}$ and $2p_{frac12}$ of phosphate (S–H, (135.98 eV, and 137.08 eV), S–$NH_2$ (132.5 eV, and 133.42 eV), S–COOH (133.3 eV, and 134.2 eV), S–H–U (133.5 eV, and 134.4 eV), S–$NH_2$–U (132.83 eV, and 133.73 eV), and S–COOH–U(134.57 eV, and 135.67 eV))[22] while the P $2p_{frac32}$ and $2p_{frac12}$ core level peaks are located in 127.73–128.46 eV and 126.63–127.36 eV, respectively in the spectra of S–H, S–H–U, and S–$NH_2$–U.[23] The spectra of S–H, S–H–U, and S–COOH–U show peak in the 132.62–133.44 eV which may be assigned to P–O–C[22] while the peak in 138.56–140.44 eV region in the spectra of S–$NH_2$, RCOOH, S–H–U, and S–$NH_2$–U were attributed to physiosorbed phosphates.[24] The HRs of S-2p of all samples are shown in Fig. 4c(i–iii). The complexity of the fitted spectra increase with changing the substitution on *ortho*-phenyl position (H<$NH_2$ and COOH). Due to spin–orbit splitting the S-2p has $2p^{\frac{1}{2}}$ and $2p^{\frac{3}{2}}$ fine structure. These fitted spectra showed a good separation ($j = 1.20 \pm 0.05$) with $2p^{\frac{3}{2}}$ having 50% of the $2p^{\frac{1}{2}}$ strength. The spectra of S–$NH_2$–U and S–COOH–U show two peaks in 167.63–168.25 eV and 168.78–169.40 eV regions corresponding to $2p^{\frac{3}{2}}$ and $2p^{\frac{1}{2}}$, respectively fo $SO_4$ group.[25] All spectra show two doublets in (168.88–169.35 eV and 170.13–170.50 eV) and (169.76–171.45 eV and 171.01–172.60 eV) corresponding to $UO_2SO_4$ and $HSO_4$ bisulfate complexes, respectively.[25,26]

The XHRs of C-1s (Fig. 5a(i–vi)) show peak around 291 eV which may be assigned to $\pi$–$\pi$* indicating an aromatic delocalized $\pi$ conjugation.[27,28] The spectra of S–COOH, S–H–U, and S–COOH–U show a peak in 283-87–283.99 eV which were attributed to α-carbon while that at in the spectra of all

compounds except S–COOH–U in the 284.10–284.79 eV were attributed to $sp^2$ hybridized carbon (C=C).[29,30] The spectrum of S–H–U show a peak at 287.15 eV which may also be assigned to C=C bond.[30] All spectra show a peak in 285.16–286.04 eV which may be attributed to C–OH[30] while that at 286.64 eV in the spectrum of S–$NH_2$–U is attributed to C–N.[31] The spectrum of S–COOH show a peak at 288.36 eV which was attributed to O=C–O.[32,33] This peak is shifted to 287.15 eV in the spectrum of S–COOH–U, which further support the coordination of carboxylate group to $UO_2^{2+}$.[22,34] All spectra show peaks in the 285.61–286.04 eV regions which are associated with $sp^2$ carbon singly bound to nitrogen, =C–NH, respectively.[29,35,36] These peaks are shifted in the spectra of S–H–U, S–COOH–U, S–$NH_2$–U, due to the change in environment arising from depredation of replaceable hydrogen (OH, NH, $NH_2$, COOH) and the formation of new bonds with $UO_2^{2+}$.

The HRs of U-4f (Fig. 5b(i–iii)) of all samples show two spin–orbit doublets in the (381.54–382.02 eV and 392.35–392.73 eV) and (383.03–384.38 eV and 393.24–395.08 eV) regions which were attributed to U-4f$_{\frac{7}{2}}$ and U-4f$_{\frac{5}{2}}$ for U(IV) and U(VI) species, respectively. The ratios of U(IV) were calculated using eqn (1) and found to be 46.30%, 86.69%, and 61.44% for S–H–U, S–$NH_2$–U, and S–COOH–U, respectively.

$$\%U^{4+} = \frac{\sum U^{4+} \text{ Peaks area(Par)of} \left( 4f_{\frac{7}{2}} + 4f_{\frac{5}{2}} \right) \times 100}{\sum U^{4+} \text{ Par} \left( 4f_{\frac{7}{2}} + 4f_{\frac{5}{2}} \right) + U^{6+} \text{ Par} \left( 4f_{\frac{7}{2}} + 4f_{\frac{5}{2}} \right)} \quad (1)$$

The HRs of N-1s of all samples are shown in Fig. 6a(i–ix). All spectra except that of S–$NH_2$, and S–COOH show a peak in the 398.04–398.75 eV region which was assigned to –N= (quinoid imine) group.[37,38] Enamine–imine tautomerism is the nitrogen analog of keto–enol tautomerism. In this process, a hydrogen atom transfers between the nitrogen atom in the enamine form Scheme S1 (SI Section II) and the ortho carbon atom of the benzene ring to generate the imine form Scheme S1 (SII). This tautomeric shift is initiated or catalyzed by the highly electropositive uranyl ion, as illustrated in Scheme S1 (SII). All spectra except that of S–H show peak in 399.28–399.64 eV region which was attributed to –NH group[37] while that of S–$NH_2$ and S–$NH_2$–U show a peak in 401.13–401.59 eV region which was assigned to –$NH_2$.[39] The spectra of S–H and S–COOH show peak in 401.39–401.96 region which was assigned to C–N group[40] while all peaks appearing at or above 402.65 eV may be attributed to charging effects, –HN$^+$– and –HN$^+$=.[41] The Spectra of S–COOH, S–$NH_2$–U and S–COOH–U show peak in 400.02–400.53 eV region which may be attributed to (=NH)$^+$[39] which further support enamine–imine tautomerism (Scheme S1 (SII)).

The XHRs of O-1s (Fig. 6b(i–vi)) show peaks in 531.03–531.75 eV and 532.35–532.88 eV regions which were attributed to –OH group[29,42] and C–O,[29,43] respectively. The spectra of S–H–U, S–COOH–U, and S–$NH_2$–U show peak in 530.67–530.80 eV region which may be attributed to metal oxygen bond/$UO_2^{2+}$
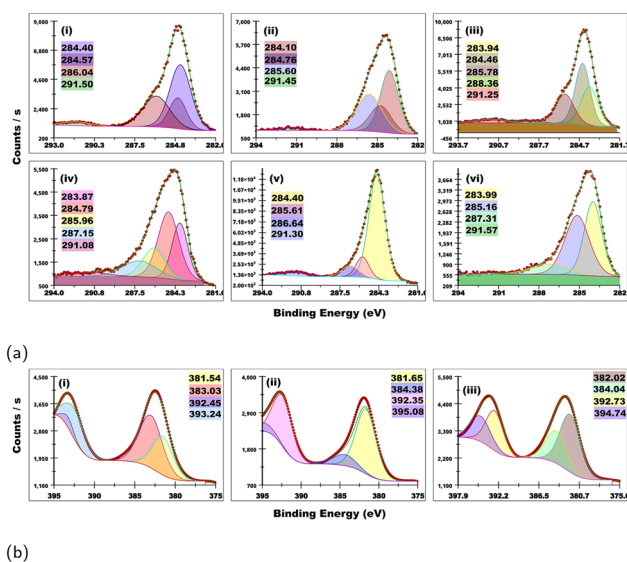


Fig. 5 (a) The XHRs of C-1s of (i) S–H, (ii) S–$NH_2$, (iii) S–COOH, (iv) S–H–U, (v) S–$NH_2$–U, (vi) S–COOH–U, (b) XHRs of U of (i) S–H–U, (ii) S–$NH_2$–U, and (iii) S–COOH–U.
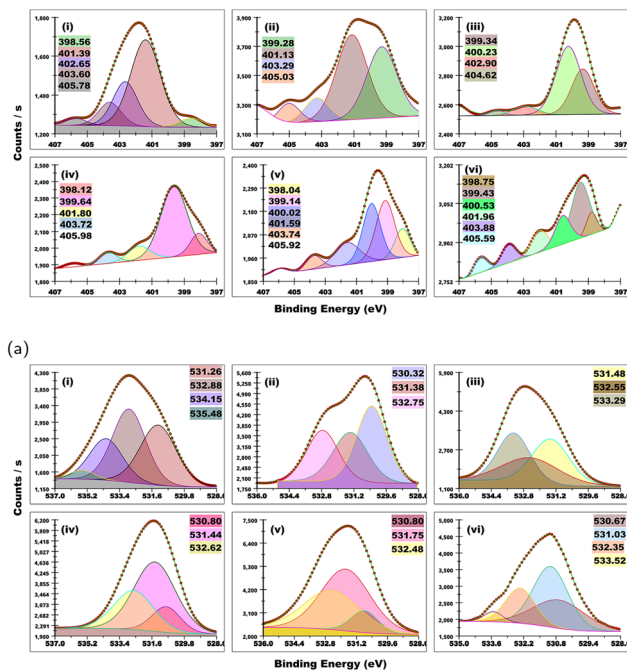
Fig. 6 (a) The HRs of N-1s of (i) S–H, (ii) S–NH$_2$, (iii) S–COOH, (iv) S–H–U, (v) S–NH$_2$–U, (vi) S–COOH–U, (b) XHRs of O-1s of ((i) S–H, (ii) S–NH$_2$, (iii) S–COOH, (iv) S–H–U, (v) S–NH$_2$–U, (vi) S–COOH–U).
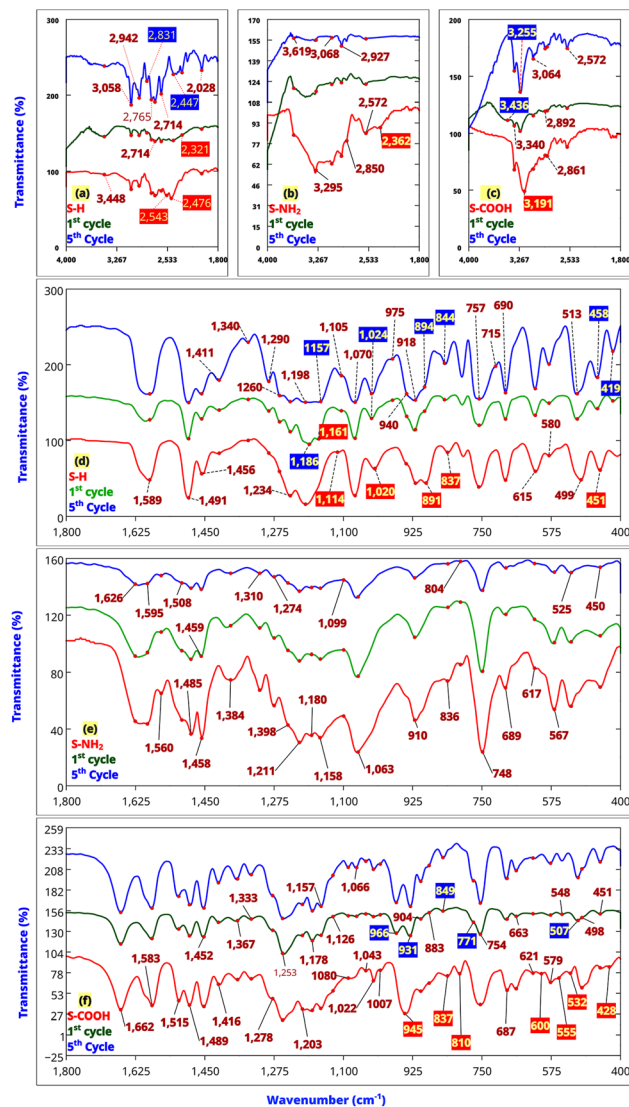


Fig. 7 FTIR of sorbents before and after 1–5 sorption/desorption cycles, 4000–1800 cm$^{-1}$: (a) SH/1/5 cycle, (b) S–NH$_2$/1/5 cycle, (c) S–COOH/1/5 cycle, 1800–400 cm$^{-1}$: (d) SH/1/5 cycle, (e) S–NH$_2$/1/5 cycle, (f) S–COOH/1/5 cycle. Note: new, shifted and disappeared peaks are highlighted blue, blue/red and red to ease the distinguishing process.

(ref. 44 and 45) and lattice oxygen (O$_\alpha$)[29,46] while the peak at 530.32 eV in the spectrum of S–NH$_2$ was assigned to surface adsorbed (O$_\beta$)/chemisorbed oxygen.[30,47] The spectra of S–COOH and S–COOH–U show a peak in 533.29–533.52 eV which was attributed to (C=O)–O.[29] The intensity of this peak decreased in the spectrum of S–COOH–U which may support coordination to the metal.[40] The spectrum of S–H show peaks at 535.48 eV and 534.15 eV which were attributed to adsorbed water and O$_\gamma$, respectively. The P–O (533.11–532.90 eV) and P=O (534.01–534.14 eV) peaks could not be located in current spectra which may be attributed to being masked by more intense peaks.[22,34]

## 3.4 FTIR

Fig. 7 shows the FTIR analysis of functional groups and stability after 1–5 sorption/desorption cycles. New (blue), shifted (blue/red), and disappeared (red) peaks are highlighted (Fig. 7a–e) to ease the distinguishing process. To fully understand the changes in spectra of sorbents before and after 1–5 sorption/desorption cycles, the 1800–400 regions were further expanded (Fig. 7d and e). The salicylaldehyde-triphenylphosphite reaction produces α-aminophosphonate, identified by diagnostic P-group FTIR signals. For example, three series of peaks are identified at 1211–1253 cm$^{-1}$ for $\nu$(–P=O),[5,6,11] 9106–945 cm$^{-1}$ for $\nu$(P–O–C), or $\nu$(P–OH),[11] and 748–757 cm$^{-1}$ for P–CH bond.[23] All sorbents showed C–N–H/N–H bending vibrations and N–H stretching vibrations in 1260–1278 cm$^{-1}$ and 1583–1595 cm$^{-1}$ region, respectively.[31,48] S–COOH and S–NH$_2$ show peaks at 1662 cm$^{-1}$ and 1626 cm$^{-1}$ which may be assigned to $\nu$(–C=O) and N–H bending vibrations.[49,50] S–H show multiple bands in 2831–3058 cm$^{-1}$ region corresponding to aryl C–H stretching vibrations, while the broad peak at 3448 cm$^{-1}$ is assigned to OH/H$_2$O group stretching vibration.[51] S–NH$_2$ show peaks at 3619, 3295, and multiple peaks between 2850-3068 cm$^{-1}$ region corresponding to OH/H$_2$O group stretching vibration, NH, and aryl C–H stretching vibrations, respectively.[51,52] S–COOH after show a peak/s in 3436–3340 cm$^{-1}$ region assignable to OH/H$_2$O group stretching vibration while the peak of –OH (benzoic acid) is shifted from 3191 cm$^{-1}$ (S–COOH) to 3255 after sorption/desorption process.[53,54] After 5 cycles, S–NH$_2$ showed the highest stability with almost no change in peaks positions. The P–CH was not affected by sorption/desorption process while the regions around –P=O and P–O–C/P–OH were more affected but retained their bond positions. IN case of S–H, the intensity of C–

N–H/N–H bending vibrations peak increased compared with –P=O peak. The sulfate ion has a regular tetrahedral structure belonging to the point group Td.[55,56] Its bivalent ionic state have two infrared active modes of vibration. When it behaves as monodentate ligand its symmetry is lowered to $C_3$, $C_{3v}$ since the oxygen atoms are no longer symmetrically equivalent showing six infrared absorption bands. A bidentate $SO_4$ group has a $C_{2v}$ symmetry with eight active modes of vibration.[55,56] S–H show new peaks at 1157 cm$^{-1}$ which masked that at 1161 cm$^{-1}$ in the sorbent. This peak at 1024 cm$^{-1}$ along with a peak overlapping with that at 615 cm$^{-1}$ may indicate the presence of traces of uncoordinated sulfate group.[57] The slight shift in other peaks in these spectra may be due to the environmental change and presence of residues. The most notable change in the spectra of S–COOH is the masking of the peak of benzene at 945 cm$^{-1}$ with the appearance of two peaks at 966 and 931 cm$^{-1}$ which may be assigned to C=C–H bending modes and waging vibration peak of –OH, respectively.[48,58,59]

### 3.5 Computational, XPS and FTIR correlations

The computationally predicted structural features provide a molecular-level explanation for the spectroscopic observations. The XPS-observed U(iv)/U(vi) ratios (S–H–U: 46.30%, S–NH$_2$–U: 86.69%, and S–COOH–U: 61.44% U(iv)) can be understood through the different binding modes predicted for each sorbent. For S–H, the predicted four-coordinate seesaw chelate at low pH evolving to six-coordinate binding at high pH explains its higher U(vi) content. The eight-coordinate complexes predicted for S–NH$_2$ at low uranium concentrations may facilitate U(iv) formation, consistent with its highest U(iv) content. The observed variations in U(iv)/U(vi) ratios among the sorbents (S–H–U: 46.30% U(iv), S–NH$_2$–U: 86.69% U(iv), and S–COOH–U: 61.44% U(iv)) can be understood through our computational findings. For S–H, calculations predict strong bidentate coordination of U(vi) through phosphonate and hydroxyl groups ($\Delta G = -157.2$ kJ mol$^{-1}$ at high pH), consistent with its higher U(vi) content. The higher U(iv) content in S–NH$_2$–U aligns with the computed eight-coordinate complex formation at low uranium concentrations, where additional NH$_2$ groups provide stabilization beyond the basic phosphonate–hydroxyl binding mode. For S–COOH, the calculations predict carboxylate involvement in uranium binding at low pH (alongside phosphonate groups), offering an explanation for the intermediate U(iv) content observed. The P-2p XPS signals show systematic shifts that correlate with the computed binding modes. The appearance of P-2p$_{\frac{3}{2}}$ and P-2p$_{\frac{1}{2}}$ peaks at 133.5 eV and 134.4 eV for S–H–U reflects phosphonate coordination to uranium, matching our computational prediction of direct P=O involvement in uranium binding. Similar correlations are seen for S–NH$_2$–U (132.83 eV, 133.73 eV) and S–COOH–U (134.57 eV, 135.67 eV), where calculations show varying degrees of phosphonate participation in uranium coordination depending on pH and concentration conditions.

For sake of characterization by IR, we note that the wavenumbers of the stretching vibrations of UO$_2{}^{2+}$, calculated at 988–1023 cm$^{-1}$, decrease upon binding to the sorbents by *ca.*

100–200 cm$^{-1}$, as detailed in the respective Fig. 1–3. The decrease is stronger at lower U concentration and at higher pH and follows the order S–H > S–NH$_2$ > S–COOH. The calculated vibrational frequencies support the FTIR observations. The predicted 100–200 cm$^{-1}$ decrease in UO$_2{}^{2+}$ stretching frequencies upon binding, most pronounced for S–H, aligns with the experimental spectral shifts. Similarly, the computed involvement of phosphonate groups in uranium binding is reflected in the observed shifts of P=O stretching bands (1211–1253 cm$^{-1}$). The experimental FTIR spectra can be directly correlated with our computational predictions. The calculations predict a decrease of 100–200 cm$^{-1}$ in UO$_2{}^{2+}$ stretching frequencies upon binding, with the magnitude of the shift following the order S–H > S–NH$_2$ > S–COOH. This trend is experimentally supported by the observed shifts in the uranyl stretching region. The computationally predicted binding modes also help explain the changes in phosphonate-related bands: the P=O stretching vibrations (1211–1253 cm$^{-1}$) show significant shifts upon uranium coordination, consistent with calculations showing direct P=O involvement in uranium binding for all sorbents. For S–H, where calculations predict the strongest uranium binding ($\Delta G = -157.2$ kJ mol$^{-1}$ at high pH) through bidentate coordination to phosphonate and hydroxyl groups, we observe the most pronounced changes in both P=O and O–H related bands. In S–NH$_2$, the computational prediction of additional stabilization through NH$_2$ groups at low uranium concentrations is reflected in the retention of N–H stretching vibrations (3295 cm$^{-1}$) alongside changes in phosphonate bands. For S–COOH, the predicted pH-dependent binding modes involving both carboxylate and phosphonate groups are supported by the concurrent changes in C=O (1662 cm$^{-1}$) and P=O stretching regions upon uranium sorption.

### 3.6 SEM-EDX analysis pre- and post-uranium sorption

The SEM images microscale images (Fig. 8) effectively validate the sorbets efficiency in uranium sorption. Images and illustrate the morphological changes in the surface structure of aminophosphonate sorbents pre- and post-uranium sorption. A
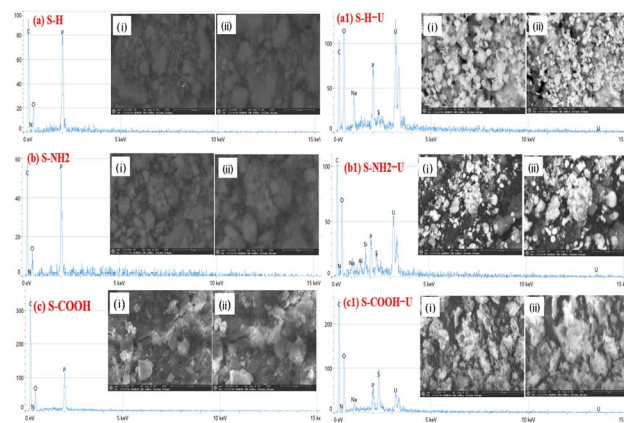


**Fig. 8** SEM-EDX images analysis of (a) S–H, (b) S–NH$_2$, (c) S–COOH, (a1) S–H–U, (b1) S–NH$_2$–U, (c1) S–COOH–U, respectively: at two different magnifications ((i) 4000× and (ii) 6000×).

detailed discussion is provided below: (a) before sorption: the sorbets' surface morphology is smooth and homogeneous, with visible porous regions indicating active binding sites. Its loosely packed particles with gaps and voids facilitate uranium ion diffusion during the sorption process. (b) After sorption: the surface appears rougher and irregular, with deposits and agglomerates visible due to uranium accumulation. Some visible pores or gaps are obscured, indicating uranium ion coverage.

A comprehensive SEM morphological analysis of the sorbents reveals the following observations: before sorption (S–H, S–NH$_2$, S–COOH):

• S–H: the surface is smooth with minimal irregularities and compact, aggregated particles.

• S–NH$_2$: similar to S–H but with slightly more porous regions, suggesting modification from the amine group.

• S–COOH: displays rougher surfaces and increased texture, likely due to the presence of the carboxylic group, enhancing surface heterogeneity.

The surface morphology of S–H–U, S–NH$_2$–U, and S–COOH–U after sorption reveals significant changes, possibly due to uranium deposition. S–NH$_2$–U shows larger clusters and increased particle density, indicating effective uranium sorption. S–COOH–U shows drastic morphological changes, becoming more granular, indicating strong interaction with uranium ions.

Generally, the increased surface roughness and visible deposits confirm successful uranium sorption, supported by EDX results showing significant uranium content. The reduced porosity indicates effective utilization of active sites, with uranium ions saturating the sorbent surface. The transformation from a smooth to a rough, compact covered surface morphology demonstrates strong interactions between uranium ions and the functional groups on the three aminophosphonate sorbents.

### 3.7 Elemental composition and purity of sorbents: EDX analysis

(Fig. 8) highlights the surface elemental composition of the sorbent, comparing its state pre- and post-UO$_2^{2+}$ sorption. The EDX spectra reveal distinct Kα signals for the common elements: P, O, N, and C at 2.02 keV, 0.53 keV, 0.39 keV, and 0.28 keV, respectively,[23] confirming the successful preparation of aminophosphonate derivatives. After UO$_2^{2+}$ loading, the Mα1, Lα1, and Lα2 signals for uranium element, appeared at approximately 3.17, 13.62, and 13.44 keV, respectively.[23] Alternatively, the appearance of a tiny Kα2 signals were identified at 1.04 keV, which is originated from the pH adjustment. Additionally, a S Kα2 signal at 2.31 keV originated from the sulfate medium, confirmed the presence of sulfate anions (SO$_4^{2-}$) linked to protonated amine sorbents' surface. This suggests the sorption of uranyl sulfate forms, indicating the involvement of anion-exchange mechanisms.[60] Notably, for S–NH$_2$, small Kα signals for Al and Si were detected at 1.49 and 1.74 keV, respectively,[23] likely due to external contamination during sample preparation, as these impurities were absent in the XPS analysis.

The EDX analysis in Table 1 provides semi-quantitative atomic percent data, showing the composition of all sorbents before uranium binding (used as a control) to track changes in elemental composition after uranium sorption. At first, a comparative analysis, functional group indicators suggest the presence of the common elements with different mass fractions based on synthesis:

• S–COOH: higher oxygen content due to carboxylate groups.

• S–NH$_2$: elevated nitrogen levels from amine groups.

• S–H: baseline elemental composition without additional functional groups.

These results strongly agree with the expected CHN/O analysis. Moreover, after U(vi) post-binding, where the C, P and N mass fractions dramatically decrease, indicating surface

**Table 1** The EDX analysis-the elemental composition (atomic% and weight%) with standard deviations (±) for all sorbents before and after UO$_2^{2+}$ sorption

| | Sorbents | | | | | | | | | | | |
| | S–H | | | | S–NH$_2$ | | | | S–COOH | | | |
| | Before | | After | | Before | | After | | Before | | After | |
| Element | [a]At% | [b]Wt% | [a]At% | [b]Wt% | [a]At% | [b]Wt% | [a]At% | [b]Wt% | [a]At% | [b]Wt% | [a]At% | [b]Wt% |
|---|---|---|---|---|---|---|---|---|---|---|---|---|
| C | 66.3 ± 0.9 | 56.4 ± 0.8 | 41.7 ± 0.8 | 18.5 ± 0.9 | 63.1 ± 1.3 | 53.8 ± 1.1 | 37.1 ± 0.7 | 18.3 ± 0.4 | 62.3 ± 0.6 | 52.9 ± 0.5 | 46.4 ± 0.6 | 30.3 ± 0.4 |
| N | 7.2 ± 4.5 | 7.3 ± 4.4 | 3.1 ± 0.3 | 1.6 ± 0.2 | 11.9 ± 3.7 | 11.8 ± 3.5 | 8.3 ± 1.4 | 4.8 ± 1.2 | 7.0 ± 1.7 | 6.9 ± 2.1 | 5.8 ± 1.4 | 5.1 ± 1.7 |
| O | 20.6 ± 1.5 | 23.3 ± 1.6 | 41.4 ± 0.9 | 24.5 ± 0.6 | 19.4 ± 1.5 | 22.1 ± 1.5 | 41.1 ± 1.1 | 27.0 ± 0.9 | 25.7 ± 1.1 | 29.1 ± 1.3 | 40.3 ± 1.1 | 36.6 ± 0.9 |
| Na | — | — | 3.3 ± 0.3 | 5.0 ± 0.2 | — | — | 2.2 ± 0.2 | 2.1 ± 0.1 | — | — | 1.5 ± 0.1 | 1.3 ± 0.1 |
| Al | — | — | — | — | — | — | 0.8 ± 0.1 | 0.9 ± 0.1 | — | — | — | — |
| Si | — | — | — | — | — | — | 1.9 ± 0.1 | 2.2 ± 0.1 | — | — | — | — |
| P | 6.0 ± 0.2 | 13.2 ± 0.3 | 3.2 ± 0.2 | 5.7 ± 0.2 | 5.6 ± 0.2 | 12.4 ± 0.4 | 2.9 ± 0.1 | 3.7 ± 0.1 | 5.1 ± 0.1 | 11.1 ± 0.2 | 2.1 ± 0.1 | 3.5 ± 0.1 |
| S | — | — | 1.9 ± 0.4 | 2.3 ± 0.1 | — | — | 1.7 ± 0.1 | 2.2 ± 0.1 | — | — | 2.3 ± 0.0 | 3.7 ± 0.1 |
| U | — | — | 5.3 ± 0.2 | 46.6 ± 0.8 | — | — | 4.0 ± 0.2 | 38.8 ± 1.9 | — | — | 1.6 ± 0.1 | 19.5 ± 0.9 |
| Total | 100 | 100 | 100 | 100 | 100 | 100 | 100 | 100 | 100 | 100 | 100 | 100 |

[a] Atomic percent (at%). [b] Weight percent (wt%).

coverage or interaction with $UO_2^{2+}$ and highlighting the active role of these groups in uranium binding.[23] Notably, the increased oxygen mass fraction in all sorbents correlates with the sorption efficiency values of uranyl ions (*i.e.*, oxyanion uranium species, $UO_2^{2+}$) presented. These changes suggest a notably higher affinity of the sorbent for $UO_2^{2+}$.

Comparative analysis of uranium sorption efficiency: S–H (5.3 atomic%): highest uranium sorption, followed by S–NH$_2$ (4.0 atomic%), and finally S–COOH (1.6 atomic%). Surprisingly, the highest and broadest U peaks in S–H–U among the other sorbents indicate superior sorption, likely due to the formation of strong chelating complexes with uranyl ions. Meanwhile, S–NH$_2$–U shows more prominent U peaks than S–COOH–U, suggesting that the amine group enhances uranium binding more effectively than the carboxylic group, through coordination and/or an ion-exchange mechanism.[7] Obviously, the sorption in S–H involves phosphonate, amine and hydroxyl groups, with high uranium content indicating strong binding affinity. S–NH$_2$ has additional amine groups, while the phosphonate groups remain dominant. S–COOH has minor carboxylic groups, which increase steric hindrance and reduce sorption efficiency. This indicates that sorption efficiency is influenced by several factors, including surface area, steric hindrance, and the impact of functionalization (S–COOH *vs.* S–NH$_2$).[7]

# 4 Conclusion

This comprehensive investigation elucidates the mechanistic intricacies underlying uranium(VI) sorption on α-aminophosphonate-based sorbents. Elemental analysis verifies three α-aminophosphonate sorbents (S–H, S–COOH, S–NH$_2$), each with unique amine-derived features. The synergistic application of multimodal spectroscopic techniques (FTIR/XPS), morphological (SEM-EDX) analysis, and DFT computations reveals that sorbent functionalization critically influences binding affinity, surface interactions, and redox behavior of uranium species. The S–H achieved maximal U(VI) sorption *via* strong synergistic P=O/–OH/–NH$_2$ coordination and optimal surface morphology. XPS analysis confirms ligand-directed U(VI) to U(IV) reduction, with S–NH$_2$–U and S–COOH–U exhibiting distinct redox stabilization *via* electronic modulation. FTIR analysis confirmed U(VI) coordination *via* P=O/N–H/C=O vibrational changes, with retained functionality after repeated sorption-desorption, proving ligand stability. Distinct uranyl surface complexes are evidenced by persistent O=U=O vibrations (FTIR) and invariant peak ratios across S–H/S–NH$_2$/S–COOH sorbents. Spectroscopic (XPS/FTIR) studies confirmed inner-sphere U(VI) complexation and ligand-mediated U(IV) stabilization at redox-active surface sites. Morphological changes observed *via* SEM-EDX, characterized by increased surface roughness and deposit formation, corroborate the effectiveness of surface immobilization mechanisms. The DFT calculations (M06-2X/defTZVP) confirm experimental observations: deprotonated functional groups at elevated pH drive exergonic U(VI) binding. These mechanistic insights guide the rational design of selective U(VI) sorbents for efficient capture and environmental remediation.

# Author contributions

A. M. A. El-Seidy: data analysis, formal analysis, software and interpretation (including XPS & FTIR studies), visualization, writing – review & editing. Ibrahim E. El-Sayed: conceptualization, resources, visualization and supervision. Mikko Linnolahtic: data curation, software and interpretation computational study (DFT studies), writing – review & editing. Hamed I. Mira, visualization, data curation, writing – review & editing. Ahmed A. Galhoum & E. E. Bayoumi: conceptualization, methodology, formal analysis, visualization, writing – original draft, writing – review & editing.

# Conflicts of interest

There are no conflicts to declare.

# Data availability

# Notes and references

1 Y. Xie, L. Yu, L. Chen, C. Chen, L. Wang, F. Liu, Y. Liao, P. Zhang, T. Chen, Y. Yuan, Y. Lu, B. Huang, H. Yang, S. Wang, S. Wang, L. Ma, F. Luo, Y. Liu, B. Hu, H. Wang, D. Pan, W. Zhu, N. Wang, Z. Wang, L. Mao, S. Ma and X. Wang, *Sci. China: Chem.*, 2024, **67**, 3515–3577.

2 M. Hao, Y. Liu, W. Wu, S. Wang, X. Yang, Z. Chen, Z. Tang, Q. Huang, S. Wang, H. Yang and X. Wang, *EnergyChem*, 2023, **5**, 100101.

3 Y. Wu, Y. Xie, X. Liu, Y. Li, J. Wang, Z. Chen, H. Yang, B. Hu, C. Shen, Z. Tang, Q. Huang and X. Wang, *Coord. Chem. Rev.*, 2023, **483**, 215097.

4 J. O. Ighalo, Z. Chen, C. R. Ohoro, M. Oniye, C. A. Igwegbe, I. Elimhingbovo, B. Khongthaw, K. Dulta, P.-S. Yap and I. Anastopoulos, *Chemosphere*, 2024, **352**, 141322.

5 E. A. Imam, A. I. Hashem, A. A. Tolba, M. G. Mahfouz, I. E.-T. El-Sayed, A. I. El-Tantawy, A. A. Galhoum and E. Guibal, *J. Environ. Chem. Eng.*, 2023, **11**, 109951.

6 E. A. Imam, I. El-Tantawy El-Sayed, M. G. Mahfouz, A. A. Tolba, T. Akashi, A. A. Galhoum and E. Guibal, *Chem. Eng. J.*, 2018, **352**, 1022–1034.

7 M. M. Rashad, I. E. El-Sayed, A. A. Galhoum, M. M. Abdeen, H. I. Mira, E. A. Elshehy, S. Zhang, X. Lu, J. Xin and E. Guibal, *Chem. Eng. J.*, 2021, **421**, 127830.

8 N. Sen, K. Saswani, K. K. Singh, S. Barkade, S. Mukhopadhyay, S. M. Chavan, S. M. Ali and K. T. Shenoy, *J. Radioanal. Nucl. Chem.*, 2017, **312**, 255–262.

9 A. A. Al-Ghamdi, A. A. Galhoum, A. Alshahrie, Y. A. Al-Turki, A. M. Al-Amri and S. Wageh, *Mater. Today Commun.*, 2022, 104536.

10 B. Kaur, P. Rana, P. Singh, A. Singh, V. Chaudhary, S. Kaya, Q. V. Le, V.-H. Nguyen and P. Raizada, *Coord. Chem. Rev.*, 2024, **518**, 216057.

11 X. Zhang, L. Zhang, Q. Wang, Q. Xin, Y. Xiong and H. Wang, *Int. J. Biol. Macromol.*, 2023, **253**, 126661.

12 Y. Zhao and D. G. Truhlar, *Theor. Chem. Acc.*, 2008, **120**, 215–241.

13 X. Cheng, *J. Chem. Thermodyn.*, 2019, **132**, 470–475.

14 A. Schäfer, C. Huber and R. Ahlrichs, *J. Chem. Phys.*, 1994, **100**, 5829–5835.

15 X. Cao and M. Dolg, *J. Chem. Phys.*, 2001, **115**, 7348–7355.

16 A. V. Marenich, C. J. Cramer and D. G. Truhlar, *J. Phys. Chem. B*, 2009, **113**, 6378–6396.

17 M. J. Frisch, G. W. Trucks, H. B. Schlegel, G. E. Scuseria, M. A. Robb, J. R. Cheeseman, G. Scalmani, V. Barone, G. A. Petersson, H. Nakatsuji, X. Li, M. Caricato, A. V. Marenich, J. Bloino, B. G. Janesko, R. Gomperts, B. Mennucci, H. P. Hratchian and J. V. Ortiz, *Gaussian 16 Revision A.03*, Gaussian Inc., Wallingford CT, USA, 2016.

18 R. F. Ribeiro, A. V. Marenich, C. J. Cramer and D. G. Truhlar, *J. Phys. Chem. B*, 2011, **115**, 14556–14562.

19 Y.-P. Li, J. Gomes, S. Mallikarjun Sharada, A. T. Bell and M. Head-Gordon, *J. Phys. Chem. C*, 2015, **119**, 1840–1850.

20 M. Mammen, E. I. Shakhnovich, J. M. Deutch and G. M. Whitesides, *J. Org. Chem.*, 1998, **63**, 3821–3830.

21 G. Luchini, J. V. Alegre-Requena, I. Funes-Ardoiz and R. S. Paton, *F1000Research*, 2020, **9**, 291.

22 X. Wu, K. Gong, G. Zhao, W. Lou, X. Wang and W. Liu, *RSC Adv.*, 2018, **8**, 4595–4603.

23 A. A. Galhoum, *Int. J. Biol. Macromol.*, 2023, **242**, 124634.

24 C. M. Navarathna, J. E. Pennisson, N. B. Dewage, C. Reid, C. Dotse, M. E. Jazi, P. M. Rodrigo, X. Zhang, E. Farmer, C. Watson, D. O. Craig, A. Ramirez, M. Walker, S. Madduri, D. Mohan and T. E. Mlsna, *Processes*, 2022, **11**, 111.

25 S. Tresintsi, K. Simeonidis, N. Pliatsikas, G. Vourlias, P. Patsalas and M. Mitrakas, *J. Solid State Chem.*, 2014, **213**, 145–151.

26 G. H. Major, J. W. Pinder, D. E. Austin, D. R. Baer, S. L. Castle, J. Čechal, B. M. Clark, H. Cohen, J. Counsell, A. Herrera-Gomez, P. Govindan, S. H. Kim, D. J. Morgan, R. L. Opila, C. J. Powell, S. Průša, A. Roberts, M. Rocca, N. Shirahata, T. Šikola, E. F. Smith, R. C. So, J. E. Stovall, J. Strunk, A. Teplyakov, J. Terry, S. G. Weber and M. R. Linford, *J. Vac. Sci. Technol.*, 2023, **41**, 038501.

27 A. Malas, A. Bharati, O. Verkinderen, B. Goderis, P. Moldenaers and R. Cardinaels, *Polymers*, 2017, **9**, 613.

28 S. R. Fouda, I. E. El-Sayed, N. F. Attia, M. M. Abdeen, A. A. H. Abdel Aleem, I. F. Nassar, H. I. Mira, E. A. Gawad, A. Kalam, A. A. Al-Ghamdi and A. A. Galhoum, *Chemosphere*, 2022, **304**, 135253.

29 A. M. El-Seidy, M. A. Elbaset, F. A. Ibrahim, S. A. Abdelmottaleb Moussa and S. A. Bashandy, *J. Trace Elem. Med. Biol.*, 2023, **80**, 127312.

30 A. M. A. El-Seidy, O. I. Sallam, I. M. Nabil, Y. S. Rammah, M. S. El-Okaily and H. Alshater, *Sci. Rep.*, 2024, **14**, 25354.

31 S. Tang, X. Yang, T. Zhang, Y. Qin, C. Cao, H. Shi and Y. Zhao, *Gondwana Res.*, 2022, **110**, 214–225.

32 S. A. E. Bashandy, A. M. A. El-Seidy, F. A. A. Ibrahim, S. S. Abdelrahman, S. A. Abdelmottaleb Moussa and M. A. ElBaset, *Sci. Rep.*, 2023, **13**, 16010.

33 A. M. A. El-Seidy, M. S. El-Okaily, I. M. Nabil and A. A. Mostafa, *Sci. Rep.*, 2025, **15**, 13714.

34 V. Uskoković, *Phys. Chem. Chem. Phys.*, 2020, **22**, 5531–5547.

35 K. Ranganathan, A. Morais, I. Nongwe, C. Longo, A. F. Nogueira and N. J. Coville, *J. Mol. Catal. A: Chem.*, 2016, **422**, 165–174.

36 A. Artemenko, A. Shchukarev, P. Štenclová, T. Wågberg, J. Segervald, X. Jia and A. Kromka, *IOP Conf. Ser.: Mater. Sci. Eng.*, 2021, **1050**, 012001.

37 G. M. Neelgund, S. F. Aguilar, M. D. Kurkuri, D. F. Rodrigues and R. L. Ray, *Nanomaterials*, 2022, **12**, 3852.

38 Y. Liu, Y. Yuan, S. Ni, J. Liu, S. Xie and Y. Liu, *Water Sci. Technol.*, 2022, **85**, 2639–2651.

39 J. K. Chaaban, N. Al Hakawati, B. Howlin, R. Bance-Soualhi and A. F. Danil de Namor, *Arabian J. Chem.*, 2020, **13**, 4824–4834.

40 M. S. Altowyan, S. M. Soliman, D. Al-Wahaib, A. Barakat, A. E. Ali and H. A. Elbadawy, *Symmetry*, 2022, **14**, 2226.

41 C. Pérez-Fernández, M. Ruiz-Bermejo, S. Gálvez-Martínez and E. Mateo-Martí, An XPS study of HCN-derived films on pyrite surfaces: a prebiotic chemistry standpoint towards the development of protective coatings, *RSC Adv.*, 2021, **11**(33), 20109–20117.

42 A. Elseidy, S. Bashandy, F. Ibrahim, S. Abd El-Rahman, O. Farid, S. Moussa and M. El-Baset, *Egypt. J. Chem.*, 2022, **65**, 497–511.

43 S. R. Masoud, S. I. Fathalla, S. M. Shawky, H. El-Gendy, M. A. Z. Alakhras, R. A. Alhotan, A. Ayyoub, S. Selim, K. D. Al-Otaibi and A. M. A. El-Seidy, *Vet. Sci.*, 2025, **12**, 333.

44 K. I. Maslakov, Y. A. Teterin, A. J. Popel, A. Y. Teterin, K. E. Ivanov, S. N. Kalmykov, V. G. Petrov, R. Springell, T. B. Scott and I. Farnan, *Appl. Surf. Sci.*, 2018, **433**, 582–588.

45 R. Khokhra, B. Bharti, H.-N. Lee and R. Kumar, *Sci. Rep.*, 2017, **7**, 15032.

46 J. Ferreira, K. Souza, F. Queiroz, I. Costa and C. Tomachuk, *Surf. Coat. Technol.*, 2016, **294**, 36–46.

47 J. Qiu, Y. Peng, M. Tang, S. Lu, X. Li and J. Yan, *Environ. Sci. Pollut. Res.*, 2021, **28**, 65416–65427.

48 G. A. A. Al-Hazmi, A. A. El-Zahhar, M. G. El-Desouky, M. A. El-Bindary and A. A. El-Bindary, *Environ. Technol.*, 2022, **45**, 731–750.

49 A. M. Borreguero, M. M. Velencoso, J. F. Rodriguez, A. Serrano, M. J. Carrero and M. J. Ramos, *J. Appl. Polym. Sci.*, 2019, **136**, 47780.

50 A. M. A. El-Seidy, E. El-Zahany, A. S. Barakat, N. S. Youssef, S. A. Galal and S. A. Drweesh, *Synth. React. Inorg., Met.-Org., Nano-Met. Chem.*, 2012, **43**, 46–56.

51 H. M. Ali, S. M. Ibrahim, E. F. Abo Zeid, A. F. Al-Hossainy and M. A. El-Aal, *RSC Adv.*, 2022, **12**, 16496–16509.

52 N. S. Youssef, E. A. El-Zahany, B. N. Barsoum and A. M. A. El-Seidy, *Transition Met. Chem.*, 2009, **34**, 905–914.

53 S. Stepanian, I. Reva, E. Radchenko and G. Sheina, *Vib. Spectrosc.*, 1996, **11**, 123–133.

54 N. S. Youssef, E. El-Zahany, A. M. El-Seidy, A. Caselli and S. Cenini, *J. Mol. Catal. A: Chem.*, 2009, **308**, 159–168.

55 M. M. Shakdofa, H. A. Mousa, A. M. Elseidy, A. A. Labib, M. M. Ali and A. S. Abd-El-All, *Appl. Organomet. Chem.*, 2018, **32**, e3936.

56 A. M. A. El-Seidy, *Synth. React. Inorg., Met.-Org., Nano-Met. Chem.*, 2014, **45**, 437–446.

57 A. S. El-Tabl, A. S. El-Tabl, M. M. E. Shakdofa, A. M. A. El-Seidy and A. N. Al-Hakimi, *Phosphorus Sulfur Silicon Relat. Elem.*, 2012, **187**, 1312–1323.

58 H. Abramczyk and W. Reimchüssel, *Chem. Phys. Lett.*, 1981, **80**, 291–294.

59 J. Jiang, Q. Zheng, Y. Yan, D. Guo, F. Wang, S. Wu and W. Sun, *Appl. Energy*, 2018, **220**, 395–407.

60 A. A. Al-Ghamdi, A. A. Galhoum, A. Alshahrie, Y. A. Al-Turki, A. M. Al-Amri and S. Wageh, *Polymers*, 2022, **14**, 2568.